A Novel RFI Source Detection Algorithm Using Array Factor Property for Synthetic Aperture Interferometric Radiometer

Bincong Liu [ORCID], Dong Zhu [ORCID], *Member, IEEE*, and Fei Hu [ORCID]

Abstract—The existence of radio frequency interference (RFI) has a great influence on the measurement of synthetic aperture interferometric radiometer (SAIR). The strong RFI signal energy picked up by the sidelobes of synthetic beam (or array factor) of SAIR easily results in false positives, deteriorating the RFI detection performance, especially when considering the representative scenes where RFIs have a large dynamic range of intensity. In this article, we propose a novel RFI source detection method by exploiting the array factor property (AFP) of SAIR. The AFP-based RFI detection method mainly consists of three steps. First, RFI sources are recovered from visibility function samples through sparse reconstruction (SR). In the recovered RFI map, the background noise is reduced and the potential RFI target regions could be extracted well. Second, the AFP of SAIR is analyzed concerning distribution characteristics of main beam and sidelobes. Based on the AFP analysis, we present a new spatial weight indicator (SWI) describing the probability of one potential RFI being a false positive. Then, an SWI-based probability map (SPM) is generated to discriminate true sources with the false positive sources. Third, the SPM and the SR-based map are combined to reconstruct the RFI image, where false positives are filtered out while true RFI sources are retained. The experiments using synthetic data and real SMOS satellite data demonstrate the effectiveness and superiority of the proposed method in RFI detection tasks for SAIR.

Index Terms—Array factor property (AFP), detection, radio frequency interference (RFI), synthetic aperture interferometric radiometer (SAIR).

I. INTRODUCTION

MICROWAVE interferometric radiometry (MIR) exploiting aperture synthesis technique has been widely used in the fields of radio astronomy, target detection, Earth observation, etc. [1], [2], [3], [4], [5], [6], [7]. The MIR can be used to retrieve geophysical parameters, such as soil moisture (SM) and sea surface salinity (SSS), facilitating weather forecasting, climate monitoring, and extreme-events prediction. A variety of instruments on MIR have been employed, such as ESTAR, GeoSTAR, microwave interferometric radiometer with aperture synthesis (MIRAS) [8], [9], [10]. In particular, the European Space Agency's Soil Moisture and Ocean Salinity (SMOS) was launched successfully in 2009, and its payload is the MIRAS, working in the L-band (1400–1427 MHz). The MIRAS receives radiation from the surface of Earth and provides a series of visibility function samples, which related to the corresponding brightness temperature (BT) map of the observed scene. The BT is essential for the retrieval of SM and SSS [11], [12].

In actual measurements, the existence of radio frequency interferences (RFIs) will significantly degrade the quality of the data products of the SMOS mission. Although 1400–1427 MHz is the protected frequency band for passive remote sensing, there are still man-made emitters occupying this frequency band and adjacent bands [13]. In the MIR, different algorithms were developed to handle RFI problems, which can be classified by the following two categories.

1) The first category is to flag and accurately localize the potential interferences during monitoring, then switch them OFF [14], [15], [16], [17].
2) The second category mainly focuses on mitigating the impact of RFI. Improved results are obtained through data processing [18], [19], [20], [21].

For either category, the accurate detection of RFI sources is crucial, because it is the prerequisite for guaranteeing RFI processing performance.

In related works, several methods can be used for the RFI detection task, including traditional direct Fourier transform (DFT) inversion [1], [22], spatial spectrum analysis [23], [24], [25], [26], and sparse signal reconstruction [27], [28]. The DFT inversion method is based on the mathematical relationship between the received visibility function and the scene BT [1], [22]. But the DFT inversion will lead to obvious Gibbs oscillations in the inverted image, and the tails around strong RFIs will interfere with the detection for other RFIs. In order to improve the detection performance for low and moderate level RFIs, Jin et al. [29] proposed the method to improve the detection process using point-source ripple function (PRF). However, this

PRF-based method still has shortcomings in handling scenes with a large dynamic of RFI intensities. For spatial spectrum analysis-based methods, previous studies proposed the idea to employ the direction-of-arrival (DOA) estimation scheme. The RFI sources are considered as target signals, and the scene signal is considered as background noise. Then, DOA estimation approaches based on the spatial spectrum analysis (e.g., MUSIC) can be applied. In detail, some researchers developed RFI detection and localization methods with direct covariance matrix (DCM) [23], [24], augmented covariance matrix (ACM) [25], and ACM completion (MCM) [26] to get improved results. However, in low SNR environments where the signal subspace and the noise subspace are mixed up, detection results will seriously deviate from ground truths. As concerns sparse signal reconstruction framework, an orthogonal matching pursuit (OMP)-based method is adopted for RFI processing [27], which obtains the representation coefficients characterizing the intensities of RFI sources. However, this OMP-based method would select incorrect atoms and expand the target support set when dealing with strong RFIs, deteriorating the detection performance. In addition, the $\ell1$-norm minimization (L1) method within the sparse reconstruction (SR) framework is proposed [28]. However, in the detection results of this method, strong RFIs signals picked up by the sidelobes are detected as additional low-intensity RFIs, which cause false alarms. In addition, the operation to suppress sidelobes would also lead to the missing alarm of low-intensity RFIs.

To address the abovementioned problems, a novel RFI source detection algorithm using array factor property (AFPRD) is proposed in this articler. The AFPRD mainly consists of three steps. First, RFI sources are recovered from visibility function samples through SR method based on reweighted $\ell1$-norm minimization (RL1). In the recovered RFI map, the background noise is reduced and the potential RFI target regions can be extracted well. Second, the AFP of SAIR is introduced concerning distribution characteristics of main beam and sidelobes. Based on the AFP analysis, we present a new spatial weight indicator (SWI) to describe the probability of a potential RFI being a false positive, which helps to discriminate the true sources with false positives. Third, each pixel in the RFI map is assigned with the SWI value to generate an SWI-based probability map (SPM). Calculating the Hadamard product of SPM and RFI maps can filter out the false positives and retain true RFI sources. The experiments using synthetic data and real SMOS data demonstrate the validity and effectiveness of the AFPRD in RFI detection tasks for SAIR, compared with commonly used methods including DFT inversion, MUSIC algorithm with DCM, ACM, and MCM matrix, and SR based on OMP and L1.

The rest of this article is organized as follows. Section II reviews the array signal model of SAIR. Section III introduces the AFPRD for details. Section IV uses synthetic data and real SMOS satellite data to prove the effectiveness of the proposed method. Finally, Section V concludes this article.

II. FUNDAMENTAL FORMULA

In this section, the array signal model of SAIR is reviewed. The output of the SAIR instrument is a series of visibility function samples, which are cross-correlations of the signals collected by two antenna [1]. In the spatial-frequency domain, the expression of the visibility function is [30]

$$V(u_{ij}, v_{ij}) = \frac{1}{\sqrt{\Omega_i \Omega_j}} \iint_{l^2+m^2 \leq 1} \frac{T_B(l,m) - T_R}{\sqrt{1-l^2-m^2}}$$
$$\cdot F_{n,i}(l,m) F_{n,j}^*(l,m) \widetilde{r}_{ij} \left(-\frac{u_{ij}l + v_{ij}m}{f_0} \right)$$
$$\cdot \exp\{-j2\pi(u_{ij}l + v_{ij}m)\} \, dl \, dm$$
$$i, j = 1, 2, \ldots, N \qquad (1)$$

where $\Omega_{i,j}$ is the equivalent solid angle of antenna; $(l,m) = (\sin\theta\cos\phi, \sin\theta\sin\phi)$ are the direction cosines; $T_B(\cdot)$ is the BT of the scene observed; $F_{n,i}(\cdot)$ represents the normalized voltage pattern of the ith element antenna; the symbol $*$ denotes the complex conjugate; $\widetilde{r}_{ij}(\cdot)$ is the fringe washing function between the ith and jth chains; f_0 is the central frequency of the receivers; N is the number of elements in the interferometric array; (u_{ij}, v_{ij}) are the spatial frequencies, also known as the baseline, which are determined by antenna positions and wavelength λ

$$u_{ij} = \frac{p_i^{(1)} - p_j^{(1)}}{\lambda}, v_{ij} = \frac{p_i^{(2)} - p_j^{(2)}}{\lambda} \qquad (2)$$

where $\left(p_i^{(1)}, p_i^{(2)}\right), \left(p_j^{(1)}, p_j^{(2)}\right)$ are position coordinates of the ith and jth antennas, respectively.

Considering that antennas are identical and receive narrowband signals, then $F_{n,i}(\cdot) = F_{n,j}^*(\cdot)$, $\Omega_i = \Omega_j = \Omega$, and the fringe washing function is negligible, i.e., $\widetilde{r}_{ij}(\cdot) \approx 1$. And the visibility function can also be written as

$$V(u_{ij}, v_{ij}) = \iint_{l^2+m^2 \leq 1} \widetilde{T}(l,m)$$
$$\cdot \exp\{-j2\pi(u_{ij}l + v_{ij}m)\} \, dl \, dm \qquad (3)$$

where the modified BT $\widetilde{T}(l,m)$ can be expressed as

$$\widetilde{T}(l,m) = \frac{T_B(l,m) - T_R}{\sqrt{1-l^2-m^2}} \cdot \frac{F_{n,i}(l,m) F_{n,j}^*(l,m)}{\sqrt{\Omega_i \Omega_j}}. \qquad (4)$$

Equation (3) reveals the Fourier-transform relationship between $V(u,v)$ and $\widetilde{T}(l,m)$, so the BT map can be inverted by an inverse Fourier transform on the visibility function, that is

$$\widetilde{T}(l,m) = \int_{-\infty}^{+\infty} \int_{-\infty}^{+\infty} V(u,v) e^{j2\pi(ul+vm)} \, du \, dv. \qquad (5)$$

From the general array processing perspective, the signal vector $\mathbf{y}$ collected by the SAIR receivers is written as

$$\mathbf{y} = \sum_{k=1}^{K} a(l_k, m_k) s(l_k, m_k) + \mathbf{n} \qquad (6)$$

where $\mathbf{y} = [y_1, y_2, \ldots, y_N]^T$, and the superscript $(\cdot)^T$ denotes the transpose operation; N denotes the number of antennas; $\mathbf{s} = [s(l_1, m_1), s(l_2, m_2), \ldots, s(l_K, m_K)]^T$ is the vector of signals from different directions; K denotes the number of signals; $\mathbf{n}$ is the noise vector; $\mathbf{A} = [a(l_1, m_1), a(l_2, m_2), \ldots, a(l_K, m_K)]$ is

the manifold matrix, which can also be written as

$$\mathbf{A} = \begin{bmatrix} e^{-j\frac{2\pi}{\lambda}(p_1^{(1)}l_1 + p_1^{(2)}m_1)} & \cdots & e^{-j\frac{2\pi}{\lambda}(p_1^{(1)}l_K + p_1^{(2)}m_K)} \\ \vdots & \ddots & \vdots \\ e^{-j\frac{2\pi}{\lambda}(p_N^{(1)}l_1 + p_N^{(2)}m_1)} & \cdots & e^{-j\frac{2\pi}{\lambda}(p_N^{(1)}l_K + p_N^{(2)}m_K)} \end{bmatrix}. \tag{7}$$

The visibility function sample is cross-correlation of each receiver channel output, which is also the covariance matrix

$$\mathbf{V} = E[yy^H] = \begin{bmatrix} E[y_1y_1^*] & \cdots & E[y_My_1^*] \\ \vdots & \ddots & \vdots \\ E[y_1y_M^*] & \cdots & E[y_My_M^*] \end{bmatrix} \tag{8}$$

where $(\cdot)^H$ denotes the conjugate transpose operation.

III. RFI DETECTION ALGORITHM USING ARRAY FACTOR PROPERTY

In this section, the process of the proposed RFI source detection algorithm using array factor property (AFPRD) method is introduced. This method is divided into three main steps, including RFI source acquisition, AFP analysis, and RFI image reconstruction. The details are discussed in the following sections.

A. RFI Source Acquisition

This section briefly introduces the basic framework of SR for RFI sources acquisition. The reason for adopting this method is because the RFIs recovered by SR can be extracted well from background. The conception of SR is based on the sparsity of RFI in the spatial distribution. At first, the covariance matrix in (8) is vectorized as

$$\mathbf{z} = \text{vec}(\mathbf{V})$$
$$= \text{vec}\left[\sum_{k=1}^{K} \sigma_k^2(\mathbf{a}(l_k, m_k)\mathbf{a}^H(l_k, m_k))\right] + \sigma_\mathbf{n}^2\overrightarrow{\mathbf{1_n}}$$
$$= \mathbf{Dq} + \sigma_\mathbf{n}^2\overrightarrow{\mathbf{1}}_n \tag{9}$$

where $\mathbf{D} = \mathbf{A}^* \odot \mathbf{A}$, and symbol $\odot$ denotes the Khatri–Rao product; $\overrightarrow{\mathbf{1}}_n$ is an N-dimensional identity matrix; σ_k^2 is the power of the kth signal, $k = 1, 2, \ldots, K$; $\mathbf{q} = [\sigma_1^2, \sigma_2^2, \ldots, \sigma_K^2]^T$ is the signal power vector.

In this article, the detection is formulated as a problem of RL1, that is,

$$\widehat{\mathbf{q}} = \arg\min_{\mathbf{q}}||\mathbf{Wq}||_1, \quad \text{s.t.} \quad ||\mathbf{z}' - \mathbf{D}^o\mathbf{q}||_2 < \delta \tag{10}$$

where δ is a positive number that determines the regularization parameter, $\mathbf{z}'$ is obtained by performing a redundancy averaging operation on $\mathbf{z}$, $\mathbf{D}^o$ is an overcomplete matrix with number of columns up to K_g, $K_g \gg K$. $\mathbf{W}$ is a K_g-dimensional diagonal matrix, whose weighting elements $\omega_m, (m = 1, 2, \ldots, K_g)$ are related to the solution vector at the previous reweighting process, as

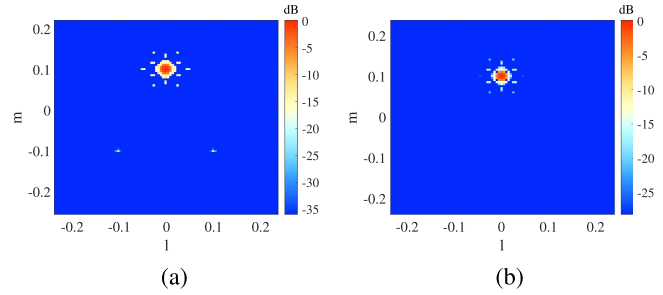$$\omega_m^{\eta+1} = \frac{1}{|q_m^\eta| + \tau} \tag{11}$$

Fig. 1. Simulation of three-RFIs scene. (a) Result recovered using RL1 method with a small denoiser parameter and (b) Result recovered using RL1 method with a large denoiser parameter.

where q_m^η is the mth element of the solution vector at the ηth reweighting process, and τ is a positive constant for solution stability.

The solved $\mathbf{q}$ is rearranged as the RFI map matrix $\mathbf{R}$. In the resulting RFI map, the target RFI regions are enhanced and background noise can be suppressed. Compared with the DFT and MUSIC methods, this feature of SR facilitates subsequent processing, mainly in RFI extraction and screening. However, within the SR framework, strong RFI signal picked up by the sidelobes can easily be detected as additional RFIs. Although the sidelobes are suppressed in the RL1 method, some false positive sources would still be detected as real in the final results. Sometimes the strength of the false positives can even exceed the strength of real RFI sources.

For example, under the condition of no background noise, we simulate three RFI sources located at $(0,0.1)$, $(-0.1, -0.1)$ and $(0.1, -0.1)$, with the intensity of 2000K, 100K, and 100K. We use denoiser parameters with different values to recover the scene, as shown in Fig. 1. Fig. 1(a) is the result for a small denoiser parameter, while Fig. 1(b) is the result for a large denoiser parameter. The results show that RL1 method could not completely eliminate the existence of false positives. Changing the denoiser parameter to better suppress the sidelobe could lead to missing detection of weak RFIs. Fig. 1(b) shows that even false positives around the strong RFI are not completely suppressed, the two weak RFIs are missed in the detection result.

B. AFP Analysis

In this section, we will introduce the derivation of AF corresponding to an SAIR system. Based on the AFP analysis, we will explain how to use AFP to filter out false positives in RFI detection. In actual measurement, as the baselines (u, v) are discrete, the measured BT $\widetilde{T}(l, m)$ can be regarded as the convolution of the actual BT $T(l, m)$ and the Fourier transform of a two-dimensional comb function, written in a compact form is

$$\widetilde{T}(l, m) = T(l, m) * F\{C(u, v)\} \tag{12}$$

where $F\{*\}$ denotes the is the Fourier transform; $C(u, v)$ is the comb function

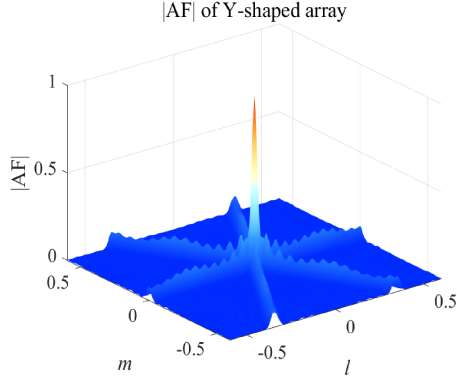$$C(u, v) = \sum_{i=1}^{i=N}\sum_{j=1}^{j=N} \delta(u - u_{ij}, v - v_{ij}). \tag{13}$$

Fig. 2. Normalized |AF| of the Y-shaped array with 69 antennas.

$F\{C(u,v)\}$ is defined as array factor [31], [32], that is

$$\mathrm{AF}(l,m) = F\{C(u,v)\}$$
$$= \sum_{i=1}^{i=N} \sum_{j=1}^{j=N} C(u,v) \exp[j2\pi(u_{ij}l + v_{ij}m)]. \quad (14)$$

It is worth noting that as the relationship shown in (12), the relative position between a strong RFI and the false positives, which result from it is consistent with the relative position between the main lobe and the sidelobes in AF. Exploiting the AFP (i.e., location feature of AF) can help to identify the false positive sources in RFI map. Based on this idea, we propose a novel RFI source detection algorithm using AFP to filter out false positive RFIs and improve detection performance.

For illustration, the AF image of Y-shaped array with 69 antennas (the minimum spacing are equal to 0.875λ) on the SMOS satellite are drawn in Fig. 2. Since AF obtained by (14) is in the plural form, the modulus of AF is taken in Fig. 2, which is denoted as |AF|. With the main lobe as the center, the sidelobes are distributed in the direction of trailing, and the intensity of sidelobes gradually weakens. The sidelobes are the reasons for false positive generation. For Y-shaped array, the number of trails is six. The same order sidelobes of different trailing directions have the same distance from the main lobe. In RFI map recovered by RL1 method, if several potential RFIs, which match the position feature of the sidelobes which appear around one RFI, these potential RFIs could be judged as false positives.

For individual detection at a distance, if RFIs exist at sidelobe locations in each trailing direction, these RFIs could be most likely false positive. However, in some actual results, due to the influence of background noise, measurement error and influences, such as the existence of other RFIs, the number of false positives occurring around an RFI is less than the sidelobe number.

To better adapt to the detection environment, a new spatial weight indicator (SWI) based on AFP is presented to characterize the probability of a potential RFI (i.e., local peaks in the RFI map) being false positive. In a single detection of a distance, a potential RFI that meets the following two conditions is defined as a suspicious RFI. First, this potential RFI appears at a sidelobe position with one RFI in the central location. Second, the intensity of the potential RFI is lower than the intensity of the RFI in the central location. During the calculation process, each potential RFI will be used to calculate SWI values with all the rest local peaks as the center, respectively. After that, the SWI value assigned to the potential RFI is the maximum SWI value. In practical terms, the larger the number of suspicious RFIs around a local peak, the higher the probability of these suspicious RFIs being false positive. We use the SWI to describe this possibility quantitatively. The appropriate calculation method of SWI can be adjusted for different detection principles. According to the observation of some existing inversion results, we find that when the number of suspicious RFIs N_s is small, the possibility of being false positive increases rapidly as N_s increases. Therefore, in this article, we adopt a power function model to construct the SWI, which can be expressed as

$$\mathrm{SWI}_{ij} = \begin{cases} \min((N_s/N_{\max})^a, 1), & i \neq j \\ 0, & i = j \end{cases}, N_s \geq 0 \quad (15)$$

where SWI_{ij} denotes the SWI value of the ith potential RFI with the jth local peak as the center, $1 \leq i, j \leq M$. M is the total number of potential RFIs; N_s is the number of suspicious RFIs; $N_{\max}$ is a constant number, which means that suspicious RFIs can be considered as false positive when N_s reaches $N_{\max}$; In subsequent calculations, $N_{\max} = 3$, which indicates that when the number of suspected RFIs around an RFI reaches or exceeds three, these suspected RFIs are judged to be false positive. Because SWI ranges from [0,1], (15) takes the minimum value between $(N_s/N_{\max})^a$ and 1; a is a constant to control growth rate, which meets the condition of $0 < a < 1$ in this model. The SWI value, which is finally assigned to the potential RFI is the maximum SWI, that is

$$\mathrm{SWI}_i = \max(\mathrm{SWI}_{ij}). \quad (16)$$

Computing SWI requires extracting the information of potential RFI from the RFI map matrix $\mathbf{R}$ ($\mathbf{R} \in \mathbb{R}^{n_1 \times n_2}$). First, a peak search is performed on $\mathbf{R}$ to obtain the spatial coordinates of all local maxima and the corresponding connected domain matrices. The connected domain matrix is defined because an RFI is internally connected. In the RFI map matrix obtained by the RL1 method, the elements in the region without RFI are zeros, while the elements in the region with RFI are nonzeros. Therefore, depending on whether the elements in the RFI map matrix are zeros or nonzeros, the connected domain matrix can be extracted to represent the distribution region of each potential RFI in the RFI map. In the connected domain matrix, the elements of the region occupied by the corresponding potential RFI are ones and the other elements are zeros. This operation is denoted as

$$(\mathbf{x}, \mathbf{y}, \mathbf{h}, \mathcal{D}) = \mathrm{traverse}(\mathbf{R}) \quad (17)$$

where $\mathbf{x} = [x_1, x_2, \ldots, x_M]^T$, $\mathbf{y} = [y_1, y_2, \ldots, y_M]^T$, and (x_i, y_i) is the coordinate of the ith potential RFI ($i = 1, 2, \ldots, M$); $\mathbf{h} = [h_1, h_2, \ldots, h_M]^T$ is the intensity vector; $\mathcal{D} \in \mathbb{R}^{n_1 \times n_2 \times M}$ is the connected domain tensor; $\mathcal{D}(:,:,i)$ is the connected domain matrix corresponding to the ith potential RFI.

Algorithm 1: SPM Calculation Algorithm Based on AFP.

Input: Recovered SR-based RFI map matrix $\mathbf{R}^{n_1 \times n_2}$, the distance from main lobe to the sidelobe d, the number of sidelobes at the corresponding distance $N_{\max}$, error tolerance δ, constant a, total number of potential RFIs M.

Output: SWI-based probability map $\mathbf{S}$.

1:    Initialization: $i = j = 1$
2:    $(\mathbf{x}, \mathbf{y}, \mathbf{h}, \mathcal{D}) = traverse(\mathbf{R})$
3:    $\mathbf{P} = zeros(M, M)$
4:    **for** $i \leq M$ **do**
5:      $N_{si} = 0$
6:      **for** $j \leq M$ **do**
7:        **if** i = j **then**
8:          $\mathbf{P}[i, j] = 0$
9:        **else if**
         $|\sqrt{(x_i - x_j)^2 + (y_i - y_j)^2} - d| \leq \delta \;\; || \;\; h_j < h_i$
         then
10:          $N_{si} = N_{si} + 1, \mathbf{P}[i, j] = 1$
11:        **end if**
12:        $j = j + 1$
13:      **end for**
14:      $\mathbf{P}[i, j] = \min((N_{si}/N_{\max})^a, 1) * \mathbf{P}[i, j], i = i + 1$
15:    **end for**
16:    $i = 1$
17:    **for** $i \leq M$ **do**
18:      $SWI_i = max(\mathbf{P}[i, :]), i = i + 1$
19:    **end for**
20:    **return** $\mathbf{S} = \sum_{i=1}^{M} SWI_i \bullet \mathcal{D}(:, :, i)$

Algorithm 2: RFI Source Detection Algorithm Using Array Factor Property Method.

Input: The samples of visibility function.

Output: The reconstructed RFI image.

1:    Step 1: Recover the RFI map matrix using the samples of visibility function by RL1 method.
2:    Step 2: Calculate the SWI value corresponding to each RFI in the RFI map and generate the SWI-based probability map (SPM).
3:    Step 3: Subtract RFI map matrix from the Hadamard product of RFI map matrix and SPM to get the RFI image.
4:    Step 4: By setting the threshold and performing a spectral peak search, the local peak beyond the threshold in the image is marked as RFI.

The information obtained above can be used to calculate SWI for each potential RFI in the RFI map recovered by the RL1 method. In the calculation result, the connected domain matrix of each potential RFI is assigned with an SWI value to represent its probability of being false positive. The SWI-based probability map (SPM) is actually a weight matrix corresponding to the RFI map matrix, which represents the probability that each potential RFI in the map is false positive. We denote SPM as $\mathbf{S}$. It can be obtained by

$$\mathbf{S} = \sum_{i=1}^{M} \mathrm{SWI}_i \bullet \mathcal{D}(:, :, i). \tag{18}$$

As summary, the process of SPM calculation algorithm based on AFP is in Algorithm 1.

C. RFI Image Reconstruction

This section introduces the procedure of using the SWI-based probability map (SPM) and the SR-based map to reconstruct the RFI image. Through Algorithm 1, all potential RFIs in the map are extracted, and the corresponding SWI value is also determined. In order to reduce the influence of false positives on detection, the intensities of potential false positives identified by the Algorithm 1 should be attenuated according to the its SWI value.

Each element in the Hadamard product matrix of the SR-based RFI map matrix $\mathbf{R}$ and $\mathbf{S}$ represents how much the corresponding pixel in the original RFI map should be attenuated. The reconstructed RFI image matrix $\mathbf{R}'$ is acquired by subtracting the Hadamard product from $\mathbf{R}$, which can be expressed as

$$\mathbf{R}' = \mathbf{R} - \mathbf{S} \odot \mathbf{R} \tag{19}$$

where $\odot$ denotes the Hadamard product.

According to $\mathbf{R}'$, the reconstructed RFI image can be drawn. Compared with previous RFI map, false positives are filtered out and real RFI sources are retained in the RFI image.

D. AFPRD Method Implementation

In this section, the procedure of the AFPRD method is summarized in Algorithm 2. In addition, we take the SMOS satellite as an example to illustrate the selection of parameters in the algorithm.

The |AF| map of MIRAS on SMOS satellite with 69 antenna elements distributed in "Y" shape (the minimum spacing are equal to 0.875λ) is as shown in Fig. 2. It can be found that the positions of the sidelobes are mainly concentrated in the direction of six trailing tails. The intensity of sidelobes gradually decays outward from the location of the main lobe. Among them, the first and second sidelobes are the first and second highest, and their height is significantly higher than the other sidelobes. Therefore, the first and second sidelobes are the main reasons for false positive generation. We simulate an RFI located at (0,0), with the intensity of 100K and the scene recovered by the RL1 method is as shown in Fig. 3. The location of false positives generated due to the first- and second-layer sidelobes can be found explicitly.

In order to effectively suppress false positives in RFI detection experiments for SMOS satellite, Algorithm 2 should be executed twice. The reason is that one kind of false positives can be filtered out in a calculation, whereas the main causes of false positives include the first and second sidelobes, which significantly higher than the other sidelobes. In the two calculations, the values of d are 0.300 and 0.475, respectively. Based on an empirical
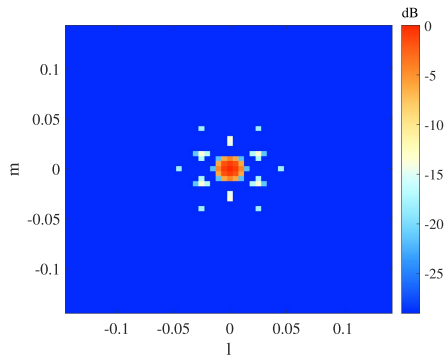
Fig. 3. Inverted scene of single RFI.

summary of the existing inversion results, the value of N_{max} is determined to be 4, and $a = \frac{2}{3}$.

IV. EXPERIMENT ANALYSIS

In this section, the performance of the proposed RFI source detection algorithm using array factor property method (AFPRD) is evaluated by simulation with synthetic data and real SMOS L1A data. Compared with the previous method, the validity is proved in the form of numerical analysis. The previous RFI detection methods used for comparison include DFT [1], [22], MUSIC algorithm with DCM, ACM, and matrix completion (denoted as DC-MUDIC [23], [24], AC-MUSIC [25], and MC-MUSIC [26], respectively), OMP [27], and L1 [28]. In addition, we separately compare detection performances of the PRF-based method [29] and the proposed AFPRD method for real RFI scenes. The choice of necessary parameters of the AFPRD are discussed in Section III-D.

A. Evaluation Indicators

This section focuses on introducing some evaluation indicators used to quantitatively evaluate performances of the AFPRD and the comparative methods. In the experiment, considering that RFI is sparse in the image, we adopted the *precision*, *recall*, and *F1-score* belonging to the evaluation indicators of the binary classification algorithm, which can be expressed as

$$\text{Precision} = \frac{\text{TP}}{\text{TP} + \text{FP}}$$

$$\text{Recall} = \frac{\text{TP}}{\text{TP} + \text{FN}}$$

$$F_1 = \frac{2 * \text{Precision} * \text{Recall}}{\text{Precision} + \text{Recall}} \quad (20)$$

where TP is the number of real RFIs, which are detected correctly (i.e., true positive); FP is the number of sources, which are falsely detected (i.e., false positive); FN is the number of RFIs that actually exist but are not detected correctly (i.e., false negative). *Precision* represents the degree of detection accuracy for RFIs detected in image, and *recall* represents the detection rate for real RFIs. In general, *precision* and *recall* are contradictory with a negative correlation. Therefore, as the harmonic mean of *precision* and *recall*, *F1-score* is considered to comprehensively

evaluate the detection performance. In addition, in order to intuitively show the detection performance of each method, we adopted the form of precision–recall (PR) curve graph in this article.

B. Experimental Analysis Using Synthetic Data

In this work, the validity of the proposed AFPRD method is proven with the synthetic data. In order to simulate the real RFI detection scene, the synthetic data is obtained by superimposing the real RFI-free scene and simulated RFIs. In experiments using single synthetic data, the data of RFI-free scene is from SMOS L1A data acquired at March 6, 2011 04:03:25 over Italy.

1) Simple RFI Scene (Scene A): In this scene, we simulate a relatively simple RFI distribution scene with a large dynamic range of RFI intensities. Six RFIs are distributed in the scene, with an intensity range of 500–8000K. The RFI images inverted by the abovementioned seven methods are shown in Fig. 4(a)–(g). The distribution image of simulated RFIs is also given in Fig. 4(h). Particularly, when performing above algorithms, the number of RFIs is assumed to be known precisely.

Fig. 4 shows the results of different methods in dealing with scene A. The result of the DFT method contains all the information of RFI, but there is a serious Gibbs oscillation phenomenon, which has a great impact on the imaging quality and RFI detection. For the DC-MUSIC in this scene, part of the signal subspace and noise subspace are difficult to distinguish effectively, and some low-intensity RFIs are difficult to find in the figure. In comparison, the image quality obtained by the AC-MUSIC and MC-MUSIC methods is higher, but the detection for some low-intensity RFIs in this scene is still unsuccessful. For OMP, the incorrect selection for atoms leads to the creation of unexpected false positives. In the image of the L1 method, all RFIs are detected, but false positives appear around the strong sources, which damage the detection performance. The proposed AFPRD suppresses the presence of false positives and had no effect on the detection of true RFIs.

On the basis of the inversion images, we normalize the results and perform a peak search. By changing the set threshold, the maximum $F1$ and its corresponding recall and precision in the inversion results of each method are listed in Table I. The reason for selecting the maximum $F1$ for comparison is that the RFI intensity obtained by the abovementioned methods is not the real RFI intensity. Therefore, it is not suitable to use the same threshold for comparison. The maximum $F1$ can quantify the best detection performance for such scene. The results show that compared with the previous methods, the AFPRD has a significant improvement in precision under the premise of ensuring the recall rate, also the best detection performance.

2) Complex RFI Scene (Scene B): In this scene, we simulate a complex RFI distribution. A total of 15 RFIs are distributed in the map, with the highest intensity of 10 000K and the lowest intensity of 500K. Compared with scene A, scene B has a larger number of RFIs and a larger power dynamic range. The RFI images recovered by the abovementioned seven methods are shown in Fig. 5(a)–(g), and the distribution image of simulated RFIs is given in Fig. 5(h). similarly, the maximum $F1$ and its
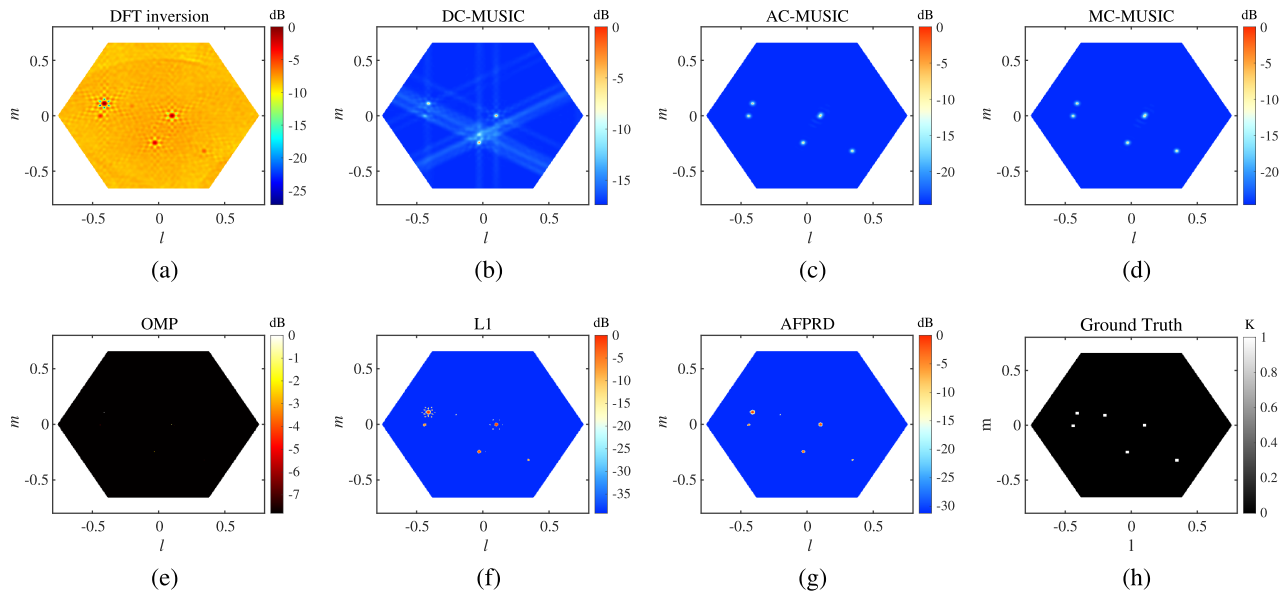
Fig. 4. Images of Scene A recovered using synthetic RFI data by (a) DFT, (b) DC-MUSIC, (c) AC-MUSIC, (d) MC-MUSIC, (e) OMP, (f) L1, (g) AFPRD, and (h) location of simulated RFIs. The proposed AFPRD method has better detection performance, which could detect all RFIs without false positives.

TABLE I
COMPARISON OF THE THREE EVALUATION INDICATORS AMONG SEVEN METHODS FOR SCENE A

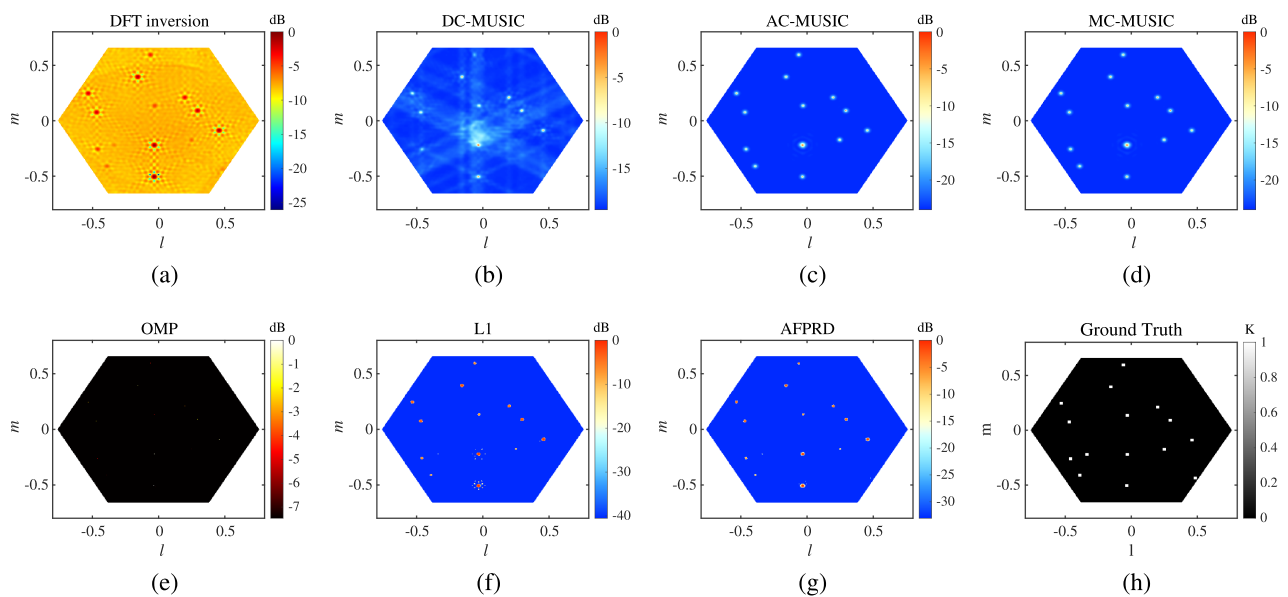| Scene A	DFT	DC-MUSIC	AC-MUSIC	MC-MUSIC	OMP	L1	AFPRD
Recall	0.6667	0.5000	0.8333	0.8333	1.0000	0.8333	1.0000
Precision	0.8000	1.0000	1.0000	1.0000	0.8571	1.0000	1.0000
$F1_{max}$	0.7273	0.6667	0.9091	0.9091	0.9231	0.9091	1.0000

Fig. 5. Images of Scene B recovered using synthetic RFI data by (a) DFT, (b) DC-MUSIC, (c) AC-MUSIC, (d) MC-MUSIC, (e) OMP, (f) L1, (g) AFPRD, and (h) location of simulated RFIs. The proposed AFP method has a better detection performance, which could detect the most RFIs on the premise of ensuring precision.

TABLE II
COMPARISON OF THE THREE EVALUATION INDICATORS AMONG SEVEN METHODS FOR SCENE B

Scene B	DFT	DC-MUSIC	AC-MUSIC	MC-MUSIC	OMP	L1	AFPRD
Recall	0.7333	0.6667	0.8667	0.8667	0.8667	0.8667	0.9333
Precision	1.0000	0.9091	1.0000	1.0000	0.9286	1.0000	1.0000
$F1_{max}$	0.8462	0.7692	0.9286	0.9286	0.8965	0.9286	0.9655

corresponding recall and precision in the inversion results of each method are also listed in Table II.

For scene B, it is worth noting that problems arising in simple scene become worse in complex scene. The severe Gibbs oscillations in the DFT result conceal the weak RFIs and affect the detection performance. For the DC-MUSIC, the precision and recall rate are greatly affected when dealing with this scene. The AC-MUSIC and MC-MUSIC guarantee the precision, but the detection for weak sources are unsatisfactory. In the image result, it can be seen that all RFIs are detected by OMP and L1. But false positives generated by strong RFIs cover up the weak sources, which reduce the recall rate. In contrast, the AFPRD has the best detection performance in this scene. Under the premise of ensuring precision, it has the highest recall rate.

3) Statistical Analysis: Without loss of generality, we use the Monte Carlo method for simulation and data analysis in multiple scenes. For both simple and complex scenes, we simulated 100 scenes with randomly distributed RFIs, respectively. Each simple scene contains six RFIs, and each complex scene contains 15 RFIs. In each scene, one third of the RFIs have intensities between 500 and 2000K; one third of the RFIs have intensities between 2000 and 7000K; and one third of the RFIs have intensities between 7000 and 10 000K. The location and intensity values of RFIs obey random distribution. In order to verify the universality of the proposed method, we consider to construct the RFI scenes with pure land background and sea-land mixed as background, respectively. In this part of the experiment, the data of land background are from SMOS L1A data acquired at March 6, 2011 04:03:25, and the data of sea-land mixed background are from SMOS L1A data acquired at August 18, 2013 00:06:58. By changing the threshold and taking the average of 100 inversion results, the PR curves of each method are drawn, as shown in Fig. 6.

Fig. 6(a) and (c) is PR curves for simple scenes with pure land as background, and Fig. 6(b) and (d) is PR curves for complex scenes with mixed sea-land as background. We can see that in these scenes, the PR curve of each method follows a similar path. Among seven methods, the PR curve of AFPRD is the highest in different backgrounds. The results show that AFPRD has a better detection performance than the abovementioned methods in scenes with a large dynamic range of RFI intensities. The superiority of the proposed method is also verified.

C. Real-Data Experiment

1) Real RFI Scene (Scene C): In this section, real SMOS data containing RFI information are used to verify the effectiveness of the proposed method. Scene C is from the SMOS L1A data at March 6, 2011 04:30:23 823.7 ms over Italy. Scene C is also recovered by abovementioned seven methods, and the results are shown in Fig. 7(a)–(g). It is worth noting that to better suppress false positives, the Algorithm 2 is looped 3 times in AFPRD. According to the position of the third sidelobe of |AF| in Fig. 2, $d_3 = 0.070$ can be determined.

It is clear that in this scene, the intensity dynamic range of the sources is large, with two strong RFIs and several weak RFIs. In the DFT image, the sidelobes of strong RFI and weak RFIs are mixed, making it difficult to distinguish them effectively. In the DC-MUSIC image, the subspace cannot be clearly divided resulting in poor imaging quality, and adjacent RFIs are treated as one. The results of AC-MUSIC and MC-MUSIC are similar, and the image quality is improved compared to DC-MUSIC. But some weak RFIs are failed to be detected. In the OMP result, all RFIs are detected but the strong RFI was incorrectly detected as several RFIs. In the L1 image, false positives appear around strong RFIs. In the result of AFPRD, the real RFIs is retained and the false positive RFIs are suppressed. This observation also demonstrates the effectiveness of the proposed method in improving the detection performance.

2) Comparative Experiment of PRF [29] and AFPRD Methods: In this section, two real scenes are selected to compare the detection performance of PRF [29] and AFPRD methods. Scene D is the scene with low- and moderate-intensity RFIs, which is from the SMOS L1A data acquired at August 18, 2013 00:26:34. Scene E is the scene with a large dynamic range of RFI intensities, which is from the SMOS L1A data acquired at August 18, 2013 00:23:08. Both scenes contain RFIs with intensities below the general decision threshold (350K). The RFIs in these two scenes are determined considering that they also occur in other snap shots of SMOS.

The reconstructed image of Scene D is shown in Fig. 8(a). In this scene, there are three RFIs with the intensities of about 566K, 385K, and 277K. In the first step of the PRF method, the RFI with intensity of 566K is detected by setting threshold as 400K. The detection result of the first step is shown in Fig. 8(b), and the detected high-intensity RFI is circled in red. In the second step of the PRF method, after removing the visibilities generated by the high-intensity RFI from the original visibilities, the detection for low- and moderate-intensity RFIs are performed on the reconstructed image. The two remaining possible RFIs are detected by setting the threshold as 250K. After multiplied by the PRF, the intensities of two possible RFIs reach 505K and 413K, respectively, both exceeding 350K. Therefore, the two possible RFIs can be correctly detected as true positives (i.e., real RFI sources). The detection result of the second step is shown in Fig. 8(c), where the detected low- and moderate-intensity RFIs are circled in red. The final detection result can be obtained by
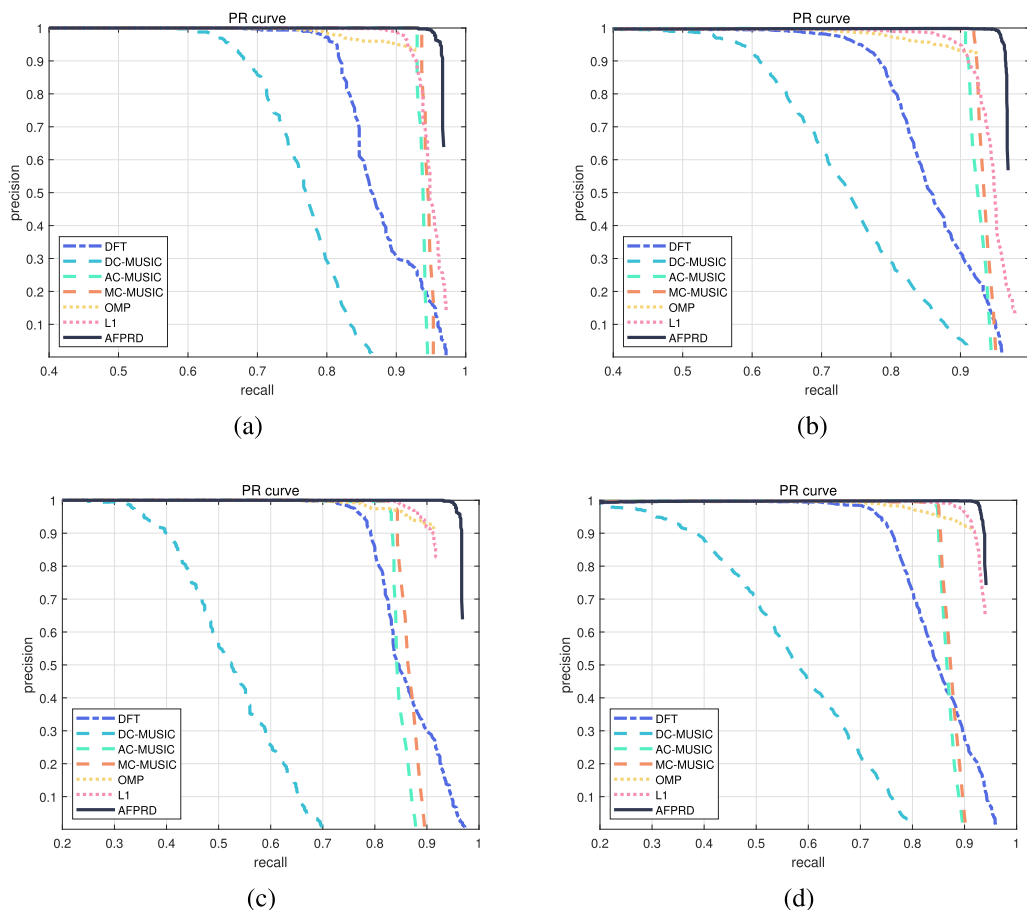
Fig. 6.   PR curves in multiple scenes of synthetic data, which are obtained by DFT, DC-MUSIC, AC-MUSIC, MC-MUSIC, RL1, and the proposed AFPRD method, respectively. (a) Simple scene with pure land as background. (b) Complicated scene with pure land as background. (c) Simple scene with mixed sea-land as background. (d) Complicated scene with mixed sea-land as background.
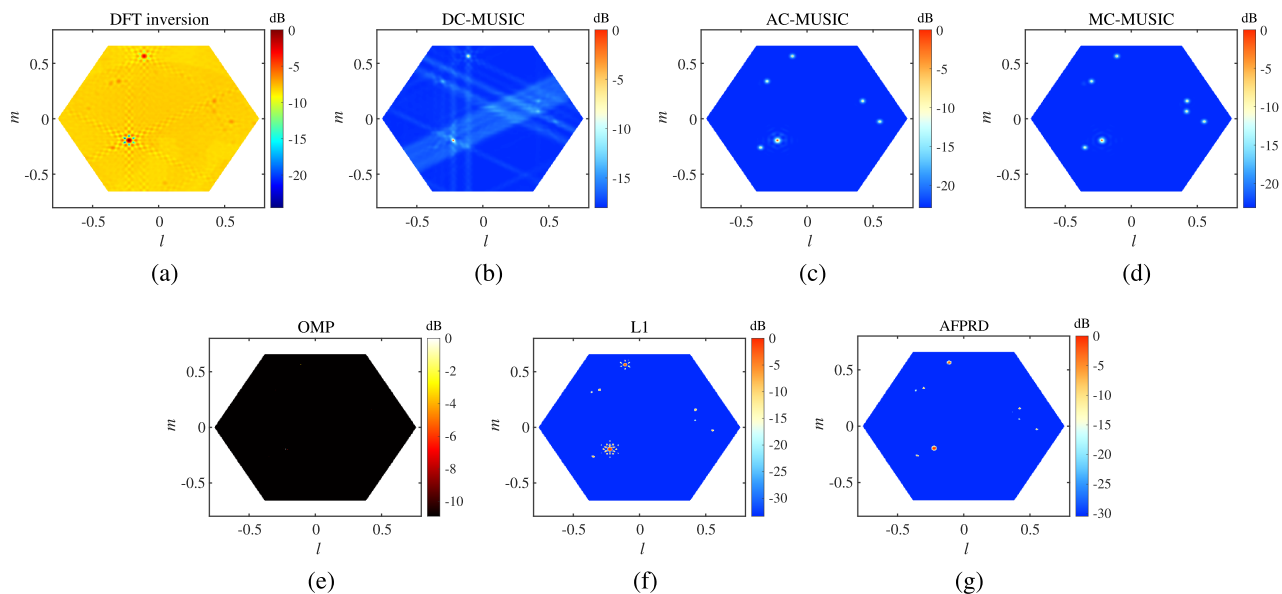

Fig. 7.   Images of Scene C recovered using real SMOS L1A data by (a) DFT, (b) DC-MUSIC, (c) AC-MUSIC, (d) MC-MUSIC, (e) OMP, (f) L1, (g) AFPRD.
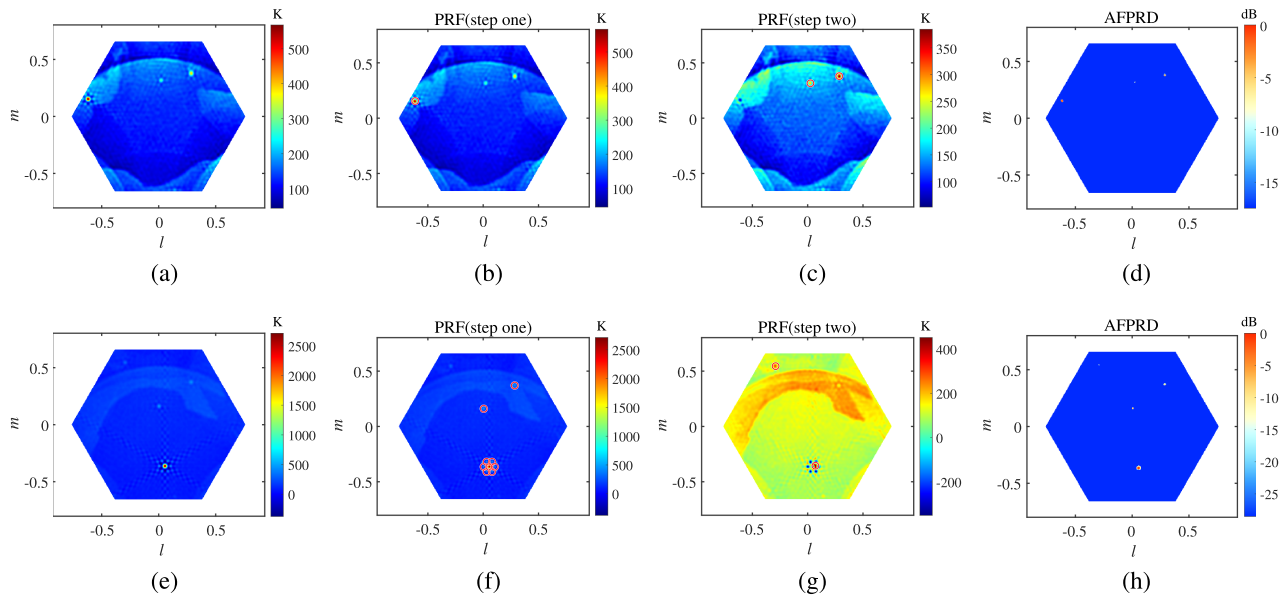
Fig. 8. RFI detection result images. (a) Reconstructed image of Scene D. (b) Result of the first step of the PRF method for Scene D, where the detected high-intensity RFI is circled in red. (c) Result of the second step of the PRF method for Scene D, where the detected low- and moderate-intensity RFIs are circled in red. (d) RFI detection result of Scene D by the AFPRD method. (e) Reconstructed image of Scene E. (f) Result of the first step of the PRF method for Scene E, where the three high-intensity RFIs detected and six false positives are circled in red. (g) Result of the second step of PRF method for Scene E, where the low- and moderate-intensity RFI detected and the false positive are circled in red. (h) RFI detection result of Scene E by the AFPRD method.

combining Fig. 8(b) and (c). All RFIs in the Scene D can be detected by the PRF method without false alarms. For comparison, the detection result obtained by the AFPRD method is shown in Fig. 8(d). As seen from the result, the AFPRD method also has a good detection performance for Scene D.

The reconstructed image of Scene E is shown in Fig. 8(e). In this scene, there are four RFIs with the intensities of about 2710K, 482K, 434K, and 304K. However, in the first step of the PRF method, nine local peaks over 400K are detected. The first sidelobes of the RFI with the intensity of 2710K are incorrectly detected as RFIs, because their intensities exceed 400K. The detection result of the first step is shown in Fig. 8(f). Similarly, three high-intensity RFIs detected and six false positives are circled in red. In the second step, after removing the visibilities generated by the high-intensity RFIs and false positives, ten possible RFIs over 250K are detected. These possible RFIs include one true RFI (304K), eight natural background fluctuations (between 250K and 260K), and one disturbance caused by incorrect visibility removal (451K). After multiplied by the PRF, the intensity of the real RFI reaches 376K, and the intensity of the disturbance reaches 856K, both of which are detected as RFIs. The intensities of the eight natural background fluctuations are below 350K and not detected as RFIs. The detection result of the second step is shown in Fig. 8(g), and the low-intensity RFI detected and the false positive are also circled in red. The final detection result can be obtained by combining Fig. 8(f) and (g). In Scene E, although all RFIs are detected by the PRF method, seven false alarms are generated at the same time. In contrast, the detection result obtained by the AFPRD method is shown in Fig. 8(h). In Fig. 8(h), all the RFI sources are detected accurately without false alarm. The result shows that the AFPRD method has a better performance in scenes with a large dynamic range of RFI intensities.

V. CONCLUSION

In this article, we propose a new RFI detection method for SAIR based on array factor property. First, RFI sources are obtained by SR. Second, we analyze the array factor property related to the occurrence of false positive sources in the inversion results, and present the SWI to describe the probability of a potential RFI being false positive. Third, the RFI image is reconstructed by combining the SWI-based map and the SR-based map. In the reconstructed RFI image, the false positives are filtered out and real sources are retained.

The effectiveness of the AFPRD is confirmed by experiments using both synthetic data and real SMOS data. For two specific scenes with a large dynamic range of RFI intensities, we compare the maximum $F1$ of AFPRD with DFT, DC-MUSIC, AC-MUSIC, MC-MUSIC, OMP, and L1. Among them, the maximum $F1$ value of AFPRD is the largest, which reveals its superiority on the detection performance of comprehensive recall and precision. In addition, in the results of the synthetic data experiments for multiple scenes, the PR curve of AFPRD is also the highest compared with other methods. Furthermore, the experiment results using real SMOS data proves that the proposed method surpass previous methods in the RFI detection performance.

REFERENCES

[1] C. Ruf, C. Swift, A. Tanner, and D. Le Vine, "Interferometric synthetic aperture microwave radiometry for the remote sensing of the earth," *IEEE Trans. Geosci. Remote Sens.*, vol. 26, no. 5, pp. 597–611, Sep. 1988.

[2] C. Zhang, H. Liu, J. Wu, W. Sun, L. Niu, and J. Yan, "A clock scanning synthetic aperture radiometer as a potential payload of sport," in *Proc. IEEE Geosci. Remote Sens. Symp.*, 2014, pp. 1929–1932.

[3] W. J. Blackwell, "Radiometer development for small satellite microwave atmospheric remote sensing," in *Proc. IEEE Int. Geosci. Remote Sens. Symp.*, 2017, pp. 267–270.

[4] A. R. Thompson, J. M. Moran, and G. W. Swenson, *Interferometry and Synthesis in Radio Astronomy*. Berlin, Germany: Springer, 2017.

[5] N. Boopath et al., "Ground-based remote sensing of soil moisture using lower frequency microwave radiometers," in *Proc. URSI Asia-Pac. Radio Sci. Conf.*, 2019, p. 1.

[6] H. Lu et al., "Ship detection by an airborne passive interferometric microwave sensor (PIMS)," *IEEE Trans. Geosci. Remote Sens.*, vol. 58, no. 4, pp. 2682–2694, Apr. 2020.

[7] Y. Cheng et al., "Regional-based object detection using polarization and fisher vectors in passive millimeter-wave imaging," *IEEE Trans. Microw. Theory Techn.*, vol. 71, no. 6, pp. 2702–2713, Jun. 2023.

[8] D. Le Vine, "Estar to SMOS: Development of interferometric radiometry for remote sensing from space," in *Proc. IEEE Int. Geosci. Remote Sens. Symp.*, 2011, pp. 3488–3490.

[9] B. Lambrigtsen, A. Tanner, T. Gaier, P. Kangaslahti, and S. Brown, "Developing a geostar science mission," in *Proc. IEEE Int. Geosci. Remote Sens. Symp.*, 2007, pp. 5232–5236.

[10] M. A. Brown, F. Torres, I. Corbella, and A. Colliander, "SMOS calibration," *IEEE Trans. Geosci. Remote Sens.*, vol. 46, no. 3, pp. 646–658, Mar. 2008.

[11] H. M. J. P. Barre, B. Duesmann, and Y. H. Kerr, "SMOS: The mission and the system," *IEEE Trans. Geosci. Remote Sens.*, vol. 46, no. 3, pp. 587–593, Mar. 2008.

[12] Y. H. Kerr et al., "The SMOS mission: New tool for monitoring key elements of the global water cycle," *Proc. IEEE*, vol. 98, no. 5, pp. 666–687, May 2010.

[13] Y. Soldo, P. de Matthaeis, and D. Le Vine, "L-band RFI in Japan," in *Proc. Radio Freq. Interference*, 2016, pp. 111–114.

[14] A. Camps, J. Gourrion, J. M. Tarongí, A. Gutierréz, J. Barbosa, and R. Castro, "RFI analysis in SMOS imagery," in *Proc. IEEE Int. Geosci. Remote Sens. Symp.*, 2010, pp. 2007–2010.

[15] E. Anterrieu, "On the detection and quantification of RFI in L1a signals provided by SMOS," *IEEE Trans. Geosci. Remote Sens.*, vol. 49, no. 10, pp. 3986–3992, Oct. 2011.

[16] Y. Soldo et al., "Localization of RFI sources for the SMOS mission: A means for assessing SMOS pointing performances," *IEEE J. Sel. Topics Appl. Earth Observ. Remote Sens.*, vol. 8, no. 2, pp. 617–627, Feb. 2015.

[17] R. Oliva, S. Nieto, and F. Félix-Redondo, "RFI detection algorithm: Accurate geolocation of the interfering sources in SMOS images," *IEEE Trans. Geosci. Remote Sens.*, vol. 51, no. 10, pp. 4993–4998, Oct. 2013.

[18] H. Park, A. Camps, M. Vall-Llossera, and V. Gonzalez-Gambau, "Strong RFI impact mitigation in the synthetic aperture interferometric radiometer," in *Proc. IEEE 15th Specialist Meeting Microw. Radiometry Remote Sens. Environ.*, 2018, pp. 1–4.

[19] Y. Soldo, A. Khazaal, F. Cabot, P. Richaume, E. Anterrieu, and Y. H. Kerr, "Mitigation of RFIS for SMOS: A distributed approach," *IEEE Trans. Geosci. Remote Sens.*, vol. 52, no. 11, pp. 7470–7479, Nov. 2014.

[20] R. Jin, Q. Li, and H. Liu, "A subspace algorithm to mitigate energy unknown RFI for synthetic aperture interferometric radiometer," *IEEE Trans. Geosci. Remote Sens.*, vol. 58, no. 1, pp. 227–237, Jan. 2020.

[21] F. Hu et al., "RFI mitigation in aperture synthesis radiometers using a modified CLEAN algorithm," *IEEE Geosci. Remote Sens. Lett.*, vol. 14, no. 1, pp. 13–17, Jan. 2017.

[22] R. Castro, A. Gutierrez, and J. Barbosa, "A first set of techniques to detect radio frequency interferences and mitigate their impact on SMOS data," *IEEE Trans. Geosci. Remote Sens.*, vol. 50, no. 5, pp. 1440–1447, May 2012.

[23] H. Park, V. González-Gambau, and A. Camps, "High angular resolution RFI localization in synthetic aperture interferometric radiometers using direction-of-arrival estimation," *IEEE Geosci. Remote Sens. Lett.*, vol. 12, no. 1, pp. 102–106, Jan. 2015.

[24] H. Park, V. González-Gambau, A. Camps, and M. Vall-llossera, "Improved music-based SMOS RFi source detection and geolocation algorithm," *IEEE Trans. Geosci. Remote Sens.*, vol. 54, no. 3, pp. 1311–1322, Mar. 2016.

[25] J. Li, F. Hu, F. He, and L. Wu, "High-resolution RFI localization using covariance matrix augmentation in synthetic aperture interferometric radiometry," *IEEE Trans. Geosci. Remote Sens.*, vol. 56, no. 2, pp. 1186–1198, Feb. 2018.

[26] D. Zhu, X. Peng, and G. Li, "A matrix completion based method for RFI source localization in microwave interferometric radiometry," *IEEE Trans. Geosci. Remote Sens.*, vol. 59, no. 9, pp. 7588–7602, Sep. 2021.

[27] D. Zhu, J. Li, and G. Li, "RFI source localization in microwave interferometric radiometry: A sparse signal reconstruction perspective," *IEEE Trans. Geosci. Remote Sens.*, vol. 58, no. 6, pp. 4006–4017, Jun. 2020.

[28] D. Zhu, H. Lu, and Y. Cheng, "RFI source detection based on reweighted ℓ1-norm minimization for microwave interferometric radiometry," *IEEE Trans. Geosci. Remote Sens.*, vol. 60, Aug. 2022, Art. no. 5301415.

[29] R. Jin, H. Lu, L. Chen, Y. Gao, and Q. Li, "Low- and moderate-level RFI detection using point-source ripple for synthetic aperture interferometric radiometer," *IEEE Trans. Geosci. Remote Sens.*, vol. 60, Feb. 2022, Art. no. 5303211.

[30] I. Corbella, N. Duffo, M. Vall-llossera, A. Camps, and F. Torres, "The visibility function in interferometric aperture synthesis radiometry," *IEEE Trans. Geosci. Remote Sens.*, vol. 42, no. 8, pp. 1677–1682, Aug. 2004.

[31] J. Bará, A. Camps, F. Torres, and I. Corbella, "Angular resolution of two-dimensional, hexagonally sampled interferometric radiometers," *Radio Sci.*, vol. 33, no. 5, pp. 1459–1473, 1998.

[32] D. Zhu, F. Hu, X. Peng, and H. Lu, "On baseline weighting for radiometric sensitivity analysis in microwave interferometric radiometry," *IEEE Antennas Wireless Propag. Lett.*, vol. 18, no. 4, pp. 791–795, Apr. 2019.

Bincong Liu was born in Hunan, China. She received the B.S. degree in electronic information science and technology from Nankai University, Tianjin, China, in 2020. She is currently working toward the master's degree in information and communication engineering with the School of Huazhong University of Science and Technology, Wuhan, China.

Her research interests include array signal processing, RFI detection, and microwave interferometric radiometers.

Dong Zhu (Member, IEEE) received the B.S. degree in communication engineering and the Ph.D. degree in electronic science and technology from the Huazhong University of Science and Technology, Wuhan, China, in 2013 and 2018, respectively.

From 2019 to 2021, he was a Postdoctoral Fellow with the Department of Electronic Engineering, Tsinghua University, Beijing, China. Since 2021, he has been a Faculty Member with the Huazhong University of Science and Technology, where he is currently an Associate Professor with the School of Electronic Information and Communications. His research interests include microwave remote sensing, array signal processing, remote sensing data processing, antenna arrays, and numerical optimization techniques for electromagnetic problems.

Fei Hu was born in Hubei, China. He received the M.S. degree in experimental mechanics and the Ph.D. degree in communication and information system from the Huazhong University of Science and Technology (HUST), Wuhan, China, in 1998 and 2002, respectively.

He was a Senior Researcher with the National Key Laboratory of Science and Technology on Multi-Spectral Information Processing Technologies, HUST. He is currently a Professor with the School of Electronic Information and Communications, HUST. His research interests include microwave technique, microwave interferometric radiometers, microwave remote sensing, and passive microwave imaging.